

# The nuclear ground-state properties and stellar electron emission rates of $^{76}\text{Fe}$ , $^{78}\text{Ni}$ , $^{80}\text{Zn}$ , $^{126}\text{Ru}$ , $^{128}\text{Pd}$ and $^{130}\text{Cd}$ using RMF and pn-QRPA models

Jameel-Un Nabi<sup>1,2</sup>, Tuncay Bayram<sup>3</sup>, Gul Daraz<sup>2</sup>, Abdul Kabir<sup>2</sup> and Şevki Şentürk<sup>3</sup>

<sup>1</sup>*University of Wah, Quaid Avenue, Wah Cantt 47040, Punjab, Pakistan*

<sup>2</sup>*Faculty of Engineering Sciences, GIK Institute of Engineering Sciences and Technology, Topi 23640, Khyber Pakhtunkhwa, Pakistan*

<sup>3</sup>*Department of Physics, Karadeniz Technical University, Trabzon, 61080, Turkey*

---

## Abstract

Our study consists of investigations of nuclear ground state properties and weak transition rates of even-even waiting point nuclei. The calculation was performed for  $N = 50$  and  $N = 82$  nuclei. The Relativistic Mean Field (RMF) model was used to explore the nuclear ground state properties of selected nuclei. The proton-neutron quasi particle random phase (pn-QRPA) model was used for the computation of allowed Gamow Teller (GT) and unique first-forbidden (U1F) transitions of the selected waiting point nuclei. The RMF approach with different density-dependent interactions, DD-ME2 and DD-PC1, was used to compute potential energy curves and surfaces, quadrupole moments, deformation parameters, binding energies, proton-neutron separation energies, charge, and radii. The RMF computed deformation parameters were used in the pn-QRPA model, as a free parameter, for the computation of GT and U1F weak transitions. We investigated three different sets of deformation parameter for the calculation of electron emission rates. The rates changed considerably with change in deformation parameter. We later investigated contribution of allowed GT and U1F rates and competition between positron capture and electron emission rates at high stellar temperatures. The computed positron capture rates were significant especially at low densities and high temperatures. The contribution of U1F rates to allowed GT appreciably reduced the total calculated half-lives. The comparison of our results with previous calculations and measurement

is also shown. The pn-QRPA calculation including U1F contribution is in good agreement with the experimental data.

*Keywords:* Gamow-Teller transitions, first-forbidden transitions, pn-QRPA model, RMF model, waiting-point nuclei, electron emission and positron capture rates

---

## 1. Introduction

The nucleosynthesis mechanism commonly referred to as rapid neutron-capture process (*r*-process) is believed to synthesize nearly half of the heavy elements beyond iron [1, 2]. Generally, the *r*-process takes place in a stellar explosive environment with a large density flux of neutrons ( $> 10^{20} \text{cm}^{-3}$ ) and high temperature ( $T \approx 10^9 \text{K}$ ) [1, 3, 4, 5]. It was observed that all nuclear matter can not be synthesized simultaneously under the same astrophysical conditions of constant temperature and density [4]. Under such a scenario, neutron capture takes place at a much faster rate than competing beta decay. The *r*-process path proceeds with the larger neutron-flux matter, that have comparatively small and approximately constant  $S_n$  (neutron separation energy). At neutron magic shell isotones with  $N = 50, 82$  and  $126$ , (also termed as waiting points) the *r*-process flow of matter slows down. The corresponding nuclei have to wait for several beta decays to occur before capturing of neutrons may resume. At these magic waiting points, the nuclear matter is accumulated, resulting in the well-known peaks in the observed *r*-process abundance distribution.

The study of closed magic shell nuclei is very crucial for a better understanding of the astrophysical *r*-process. Due to their stronger binding energies, the neutron separation energies show discontinuities at these magic shell nuclei [6, 7], resulting in rather low neutron capture rates. As a consequence the *r*-process matter flow moves closer to stability, where nuclei have substantially larger EE half-lives. Thus matter accumulates around closed shell nuclei with  $N=50, 82$ , and  $126$ , producing the observed peaks in the *r*-process distribution. The open shell nuclei become abundant in comparison to their closed shell counterparts as the shell effects disappear [8]. Our present calculations are only applicable to even-even closed shell waiting points. However, in future we will extend our investigations to open shell nuclei in order to provide a complete coverage for *r*-process simulation studies.

The half-lives ( $T_{1/2}$ ) of electron emission (EE) calculation have a considerable impact on the dynamics of  $r$ -process and abundance distribution. The calculated  $T_{1/2}$  of EE transitions of waiting points nuclei describes the time scale it takes the mass flow to transpose seed nuclei to larger ones in the third peak around  $A \sim 200$ . The available data for the EE half-lives of closed shell waiting points is insufficient [9, 10, 11] and requires attention of theorists and experimentalists. The radioactive ion beam facilities (e.g. RIKEN [12] and FAIR-GSI [13]) will improve the scenario in near future. The required half-lives for the simulation of  $r$ -process primarily come from theoretical investigations [14].

For the investigation of some fundamental nuclear ground state properties of even-even waiting point isotones with  $N = 50$  and  $82$ , we employed the Relativistic Mean Field (RMF) approach in axially deformed shape with different density-dependent interactions. The RMF model is a phenomenological approach for description of various ground-state nuclear properties of nuclei and it describes nuclei at hadronic degrees of freedom. It was first introduced as a fully fledged quantum field theory by Walecka [15]. Later, an additional density dependence has been added in the RMF theory for quantitative and correct description of surface properties of nuclei [16]. It has been applied to obtain nuclear properties of nuclei not only in stability but also far from stability [17, 18, 19, 20, 21, 22, 23, 24, 25, 26].

Nuclei with proton number  $Z = 40 - 50$  and neutron number  $N = 82$  are close to neutron drip-line. We investigate ground-state nuclear properties for these isotones by using the RMF model with density-dependent interactions because RMF model is successful in describing ground-state properties of nuclei far from stability line. The potential energy curves (PECs) and the potential energy surfaces (PESs) of selected nuclei was performed. The quadrupole deformation parameter, calculated within the framework of RMF model, was later used in the pn-QRPA model as a free parameter.

We further investigate the allowed Gamow-Teller GT and unique first-forbidden U1F stellar weak electron emission rates ( $\lambda_{EE}$ ) for  $N = 50$  and  $82$  isotones by employing the pn-QRPA model with a deformed Nilsson potential basis. The first attempt to calculate the microscopic weak interaction rates for a large number of available nuclei, far away from the stability line was performed by Klapdor et al. [27] by using the pn-QRPA approach. Later on these calculations were refined by Staudt et al. [28, 29] and Hirsh et al. [30] employing the same nuclear model. Nabi and Klapdor-Kleingrothaus, for the first time, employed a deformed pn-QRPA model with schematic separable

interaction and calculated the stellar weak rates of  $sd$ ,  $fp$  and  $fp$ -shell nuclei under astrophysical conditions of temperature and density [31, 32, 33]. This approach provides a state-by-state calculation of weak transition rates in a microscopic fashion.

For  $N = 50$  and 82 isotones, the past theoretical calculations of EE rates are overall in decent comparison with available measured data [34, 35]. The important reason for disagreement between different theoretical calculation is that they did not take into account the computation of first-forbidden (FF) transitions. The presence of single-particle energy states with different parities can lead to a significant impact on calculated half-lives. The forbidden transitions possess a decent contribution for the  $N = 50$  and 82 isotones. In this regard, Homma et al. [36] made a first effort to include the contribution of unique first-forbidden (U1F) weak rates to the total rates by using the pn-QRPA approach. Borzov, recently computed the FF inclusion to the total weak rates by using self-consistent density-functional+continuum QRPA approach [37]. His study shows a substantial reduction of total half-lives with the inclusion of FF transitions for waiting point isotones. The FF inclusion was also calculated by using the large scale shell model (LSSM) [35].

The authors in Ref. [38] employed fully self-consistent covariant density functional theory (CDFT) for the ground and excited states of nuclei. The  $\beta$ -decay half-lives and neutron emission probabilities were calculated for a large number of nuclei. The FF transitions were found to contribute significantly to the total decay rates. More recently the FF contribution was studied by using the deformed pn-QRPA theory for neutron rich nuclide in stellar matter by [39].

In this paper we plan to investigate nuclear structure properties of  $N = 50$  and 82 isotones using the RMF model. We later employ the pn-QRPA model for the computation of weak rates and half-lives of selected waiting points.

Section 2 describes briefly the necessary formalism. Results of our calculations and comparison with previous results and measurement are discussed in Section 3. We finally conclude our findings in Section 4.

## 2. Theoretical Framework

### 2.1. The RMF Model

The RMF model based calculations are described in such a way that nucleons interact with each other with exchange of various mesons and photon.

We only consider  $\sigma$ ,  $\omega$  and  $\rho$  mesons in our model. One can find few types of non-linear RMF model based on handling of self-interaction of mesons and density-dependent meson-nucleon couplings (for further follow-up see Ref. [20] and references therein). The RMF model based density-dependent meson-nucleon couplings is described shortly in this subsection. The RMF model starts with phenomenological relativistic Lagrangian density given as

$$\begin{aligned} \mathcal{L} = & \bar{\psi}(i\gamma\partial - m)\psi + \frac{1}{2}(\partial\sigma)^2 - \frac{1}{2}m_\sigma\sigma^2 - \frac{1}{4}\Omega_{\mu\nu}\Omega^{\mu\nu} \\ & + \frac{1}{2}m_\omega^2\omega^2 - \frac{1}{4}\vec{R}^{\mu\nu}\vec{R}_{\mu\nu} + \frac{1}{2}m_\rho^2\vec{\rho}_\mu^2 - \frac{1}{4}F^{\mu\nu}F_{\mu\nu} - g_\sigma\bar{\psi}\sigma\psi \\ & - g_\omega\bar{\psi}\gamma_\mu\omega\psi - g_\rho\bar{\psi}\gamma_\mu\vec{\rho}\vec{\tau}\psi - e\bar{\psi}\gamma_\mu A^\mu\psi. \end{aligned} \quad (1)$$

The  $\psi$  is Dirac spinor and it represents nucleon with mass  $m$ . The  $m_\sigma$ ,  $m_\omega$  and  $m_\rho$ , are the masses of  $\sigma$ ,  $\omega$  and  $\rho$  mesons, respectively.  $g_\sigma$ ,  $g_\omega$  and  $g_\rho$  represent the coupling constants for the mesons to the nucleon. The field tensors of  $\omega$ ,  $\rho$  and the photon were expressed as

$$\begin{aligned} \mathbf{\Omega}^{\mu\nu} &= \partial^\mu\omega^\nu - \partial^\nu\omega^\mu, \\ \vec{\mathbf{R}}^{\mu\nu} &= \partial^\mu\vec{\rho}^\nu - \partial^\nu\vec{\rho}^\mu, \\ \mathbf{F}^{\mu\nu} &= \partial^\mu A^\nu - \partial^\nu A^\mu. \end{aligned} \quad (2)$$

In these equations vectors in three-dimensional space are shown with bold-faced symbols where in the isospin space the vectors are represented in conventional symbol having overhead arrows. The unknown meson masses and coupling constants are parameters and they are fine-tuned by using known experimental data to its correct predictions of nuclear matter properties and ground-state properties of finite nuclei. The meson-nucleon vertex functions can be fixed-on by tuning the parameters of the assumed phenomenological density dependence of the meson-nucleon couplings to regenerate the properties of symmetric and asymmetric nuclear matter and finite nuclei as reported in Ref. [40].

Tacking into account the classical variational principle, the equations of motion for the fields can be derived from the relativistic Lagrangian density given in Eq. (1). A set of coupled equations (Dirac equation with the potential terms for the nucleons) and the Klein-Gordon like equations with

sources for mesons and photon are obtained. The set of these equations can be solved separately by the expansion of the wave functions in terms of a spherical, an axially and a triaxially symmetric harmonic oscillator potential [41]. In the present study, axially and triaxially symmetric RMF calculations have been performed to obtain ground-state nuclear properties of  $^{76}\text{Fe}$ ,  $^{78}\text{Ni}$ ,  $^{80}\text{Zn}$ ,  $^{126}\text{Ru}$ ,  $^{128}\text{Pd}$  and  $^{130}\text{Cd}$  nuclei as well as to obtain their PECs and PESs by following the recipe of Ref. [41]. In the present calculation we employ two different types of density-dependent interactions namely DD-ME2 [40] and DD-PC1 [42]. We took into account 12 shells for neutrons and protons. No convergence problem was witnessed in our iterative calculations.

## 2.2. The $pn$ -QRPA model

Our calculation involves solution of  $pn$ -QRPA equations in a multi-shell single-particle space with a schematic interaction. The Hamiltonian of the model is given by

$$H^{QRPA} = H^{sp} + V^{pair} + V_{GT}^{ph} + V_{GT}^{pp}. \quad (3)$$

Single particle energies and wave functions were calculated in the deformed Nilsson potential basis. Pairing was treated within the BCS formalism. The calculated EE transitions and related half-lives strongly depend on the Q-values and residual interactions [43]. The residual interactions  $\chi$  ( $ph$ ) and  $\kappa$  ( $pp$ ), known as particle-hole part and particle-particle part respectively, were considered for the computation of both allowed GT and U1F calculation. For a detailed description of  $\chi$  and  $\kappa$  and optimum choice of these parameters we refer to [29, 30, 36]. For the U1F transitions, the  $pp$  and  $ph$  matrix elements are given by

$$V_{pn,p'n'}^{ph} = +2\chi_{U1F} f_{pn}(\mu) f_{p'n'}(\mu), \quad (4)$$

$$V_{pn,p'n'}^{pp} = -2\kappa_{U1F} f_{pn}(\mu) f_{p'n'}(\mu), \quad (5)$$

where

$$f_{pn}(\mu) = \langle p | t_{-r} [\sigma Y_1]_{2\mu} | n \rangle, \quad (6)$$

represents the single particle transition amplitude between Nilsson single particle states.  $\mu$  represents the spherical component of the transition operator and takes the value of 0,  $\pm 1$  and  $\pm 2$ . The neutron and proton states possess different parities. Other input parameters for computation of weak transitions are pairing gaps ( $\Delta_p$ ,  $\Delta_n$ ), nuclear deformation ( $\beta_2$ ) values, Q-values

and Nilsson potential parameters (NPP). We performed our calculation by using the nuclear deformation parameter from the recent global calculation of finite range droplet model (FRDM) [45]. The NPP were adopted from [46] and the oscillation constant (identical for both of protons and neutrons) was determined using the relation  $\hbar\omega = 41A^{-13}$  [MeV]. We used the Nilsson potential for the calculation of wave function. The Nilsson model has been widely used to describe the structure of low-lying states. The nuclear deformation parameter  $\beta_2$  was used as an input parameter in the Nilsson potential in our computation. As a starting point, single particle energies and wave functions were computed in the deformed Nilsson basis. The transformation from the spherical nucleon basis ( $c_{jm}^+$ ,  $c_{jm}$ ) to the axial symmetric deformed basis ( $d_{m\alpha}^+$ ,  $d_{m\alpha}$ ) were performed using

$$d_{m\alpha}^+ = \sum_j D_j^{m\alpha} c_{jm}^+, \quad (7)$$

where  $d^+$  and  $c^+$  indicate the particle creation operators in the deformed and spherical basis, respectively. The transformation matrix  $D_j^{m\alpha}$ , is a set of Nilsson eigen-functions with  $\alpha$  as an additional quantum number which describes the Nilsson eigen-states. The BCS formalism was used in the Nilsson basis for neutron/proton system separately. The transformation matrices were determined by diagonalization of the Nilsson Hamiltonian (for complete description we refer to [30, 47]).

Pairing gap values,  $\Delta_n = \Delta_p = 12/\sqrt{A}$  [MeV], was used in our calculation according to the global systematic. The Q-values were taken from the recent atomic mass data evaluation of [48].

Details of solution of the Hamiltonian shown in Eq. (3) may be studied from [49]. Calculation of terrestrial EE half-lives may be seen from [29]. Also, the formalism used for the estimation of allowed GT and U1F transitions in stellar scenario by using pn-QRPA approach can be studied in more details from Refs. [32, 33, 50, 51].

The allowed positron capture (PC) rates from the parent nucleus  $i$ th-state to the daughter nucleus  $j$ th-state is specified by

$$\lambda_{ij}^{(PC)} = \frac{\ln 2}{D} [f_{ij}(T, \rho, E_f)] [B(F)_{ij} + \left(\frac{g_A}{g_V}\right)^2 B(GT)_{ij}]. \quad (8)$$

The value of  $D$  is taken as 6143 s [52]. In above equation ( $B_{ij}$ )s depict the reduced transition probabilities of Fermi ( $B(F)$ ) and GT ( $B(GT)$ ) interactions. We took the value of  $g_A/g_V$  (ratio of weak axial and vector coupling

constant) to be  $-1.2694$  [53]. The same value was taken for the calculation of weak transition rates of neutron rich Cu-isotopes in stellar matter. The authors in Ref. [35] used the value  $g_A/g_V = -1.2701$  for the closed magic shell nuclei of  $N= 50, 82$  and  $126$ . Detail formalism for computation of allowed capture rates in stellar environment can be studied in [32].

The U1F stellar EE and PC rates from  $i$ th-state of the parent to  $j$ th-state of the daughter nucleus is specified by

$$\lambda_{ij}^{EE(PC)} = \frac{m_e^5 c^4}{2\pi^3 \hbar^7} \sum_{\Delta J^\pi} g^2 f_{ij}(\Delta J^\pi) B_{ij}(\Delta J^\pi), \quad (9)$$

where  $f_{ij}(\Delta J^\pi)$  is the integrated Fermi function and  $B_{ij}(\Delta J^\pi)$  is the reduced transition probability for weak EE and capture rates. ( $g$ ) in the expression is the weak coupling constant. The weak coupling constant ( $g$ ) take the values of  $g_V$  or  $g_A$  based on  $\Delta J^\pi$  transitions. The dynamics part of the rate equation is given by

$$B_{ij}(\Delta J^\pi) = \frac{1}{12} \zeta^2 (w_m^2 - 1) - \frac{1}{6} \zeta^2 w_m w + \frac{1}{6} \zeta^2 w^2, \quad (10)$$

where  $\zeta$  is

$$\zeta = 2g_A \frac{\langle f || \sum_k r_k [\mathbf{C}_1^k \times \sigma]^2 \mathbf{t}_-^k || i \rangle}{\sqrt{2J_i + 1}}, \quad (11)$$

and

$$\mathbf{C}_{lm} = \sqrt{\frac{4\pi}{2l+1}} \mathbf{Y}_{lm}, \quad (12)$$

with  $\mathbf{Y}_{lm}$  the spherical harmonics. The kinematics portion of Eq. (9) can be obtained as

$$f_{ij} = \int_1^{w_m} w \sqrt{w^2 - 1} (w_m - w)^2 [(w_m - w)^2 F_1(Z, w) + (w^2 - 1) F_2(Z, w)] (1 - D_-) dw, \quad (13)$$

the term ( $w$ ) relates to the overall kinetic energy of the electron with the inclusion of its rest-mass energy. The mathematical expression  $w_m = m_p - m_d + E_i - E_j$  represents the total energy of corresponding weak electron emission-decay. Here the terms  $m_p$  and  $E_i$ , relates the mass and excitation energies ( $E_{xp}$ ) of the parent nucleus, respectively. Whereas,  $m_d$  and  $E_j$  are the related mass and excitation energies of the daughter nucleus, respectively. The distribution function for the electrons is shown by  $D_-$ . We assume that



electrons are not residing in a bound state, and following the Fermi-Dirac distribution functions,

$$D_- = [\exp(\frac{E - E_f}{kT}) + 1]^{-1}. \quad (14)$$

In the above expression,  $E = (w - 1)$  and  $E_f$  indicates the K.E (kinetic energy) and fermi energy ( $E_f$ ) of electrons, respectively.  $T$  is the temperature in units of Kelvin-scale and the term  $k$  implies for the Boltzmann constant. We refer to and study the recipe of [54] for calculation of Fermi functions,  $F_1(\pm Z, w)$  and  $F_2(\pm Z, w)$  shown in equation (Eq. (13)).

Due to the presence of high temperatures in stellar core, EE and capture rates have a small contribution from parent excited energy levels. We use the Boltzmann distribution function to calculate the occupation probability of parent *ith*-state is

$$P_i = \frac{\exp(-E_i/kT)}{\sum_{i=1} \exp(-E_i/kT)}. \quad (15)$$

The total stellar EE and PC rates were finally calculated by using

$$\lambda^{EE(PC)} = \sum_{ij} P_i \lambda_{ij}^{EE(PC)}. \quad (16)$$

The summation stands for computation of all parent and daughter energy levels until required and desire convergence is achieved. We found that due to the presence of large model space (about up to  $7\hbar\omega$  major oscillatory shells) desire convergence can be easily obtained in our weak EE and PC computations. This is one of the big success of pn-QRPA approach as it may be employed for computation of weak rates of any arbitrary heavy nuclear-species.

### 3. Results and discussion

We first discuss the results obtained from the axially deformed RMF-model with different density interaction parameters. The calculated binding energies of  $N = 50$  ( $^{76}\text{Fe}$ ,  $^{78}\text{Ni}$ ,  $^{80}\text{Zn}$ ) and  $N = 82$  ( $^{126}\text{Ru}$ ,  $^{128}\text{Pd}$ ,  $^{130}\text{Cd}$ ) nuclei by using RMF model with DD-ME2 and DD-PC1 interactions are shown in Fig. 1. The results of binding energies for these nuclei employing the RMF model with non-linear NL3\* interaction parameters [23], Hartree-Fock

Bogoliubov (HFB) theory with Sly4 parameter set [55], finite-range droplet model (FRDM) [45] and available experimental data [57] are also shown for comparison. Maximum deviations of binding energies from available experimental data ( $^{78}\text{Ni}$ ,  $^{80}\text{Zn}$ ,  $^{128}\text{Pd}$  and  $^{130}\text{Cd}$  nuclei) for RMF[DD-ME2], RMF[DD-PC1], RMF[NL3\*], HFB[Sly4] and FRDM are between 0.024 – 0.049 MeV, 0.004 – 0.027 MeV, 0.011 – 0.027 MeV, 0.006 – 0.037 MeV and 0.012 – 0.025 MeV, respectively. The results indicate that the ground-state binding energies of the nuclei obtained from the RMF model with DD-ME2 interaction are much closer to the experimental results.

Nucleon separation energies for one-neutron ( $S_n$ ), one-proton ( $S_p$ ), two-neutron ( $S_{2n}$ ) and two-proton ( $S_{2p}$ ) for the corresponding waiting points by using RMF model with DD-ME2 and DD-PC1 interactions are shown in Fig. 2. The results of RMF model with NL3\* interaction [23], HFB theory with SLy4 interaction [55], FRDM [45] and experimental data [57] are also shown in Fig. 2 for comparison. As seen in Fig. 2a and Fig. 2b, the results of FRDM for  $S_n$  and  $S_p$  separation energies of selected nuclei are much closer to available experimental data. The maximum deviation between the experimental data and the results of RMF model with DD-ME2 and DD-PC1 interactions is under 1 MeV. The same success of FRDM model in describing  $S_{2n}$  and  $S_{2p}$  energies of selected nuclei is seen in Fig. 2c and Fig. 2d. On the other hand, the RMF model with DD-ME2, DD-PC1 and NL3\* interactions and HFB theory with SLy4 interaction provide compatible results.

Accurate knowledge of neutron skin thickness ( $\Delta r_{np} = r_n - r_p$ ) is important for problems in the field of nuclear physics and astrophysics. As an example case, the slope parameter of symmetry energy of nuclear matter is correlated with the neutron skin thickness [58]. In Fig. 3, calculated neutron skin thickness of  $^{76}\text{Fe}$ ,  $^{78}\text{Ni}$ ,  $^{80}\text{Zn}$ ,  $^{126}\text{Ru}$ ,  $^{128}\text{Pd}$  and  $^{130}\text{Cd}$  nuclei by using RMF model with DD-ME2 and DD-PC1 interactions are shown. The predictions of RMF model with NL3\* parameter set [23] and HFB theory with SLy4 interaction [55] are shown for comparison. As it is well known from our fundamental nuclear physics knowledge, neutron skin thickness decreases by adding proton in an isotonic chain of nuclei. This case is clearly visible for  $N = 50$  and  $N = 82$  isotonic chains in Fig. 3. It may be understood from the figure that the RMF model and HFB theory give close results to each other for neutron skin thickness of the selected nuclei. It may be further noted that the results of RMF model with NL3\* differ from those of others while its tendency for adding protons is same.

Experimentally, the root-mean-square (rms) charge radius of a nucleus

is measured by using the interactions between the nucleus and electrons or muons. One can find experimental methods for determination of rms charge radii of a nucleus along stability line and far away from the stability line [59]. Latest compiled experimental charge radii data of nuclei can be found in Ref. [60]. There is no available experimental data for rms charge radii of  $^{76}\text{Fe}$ ,  $^{78}\text{Ni}$ ,  $^{80}\text{Zn}$ ,  $^{126}\text{Ru}$ ,  $^{128}\text{Pd}$  and  $^{130}\text{Cd}$  because these nuclei are close to the neutron dripline. On the other hand some empirical charge radii formulae, where parameters are fitted by using known experimental data, works well [61]. One of the latest refitted empirical charge radii formulas by using the data of 898 nuclei is

$$R_c = \sqrt{5/3}((r_p Z^{1/3})^2 + 0.64)^{1/2}, \quad (17)$$

where  $r_p$  and  $Z$  are proton radii and proton numbers of nuclei, respectively. This formula gives the smallest root-mean-square deviation with respect to other empirical charge radii formulae. Details can be found in Ref. [61]. In Table 1, the calculated nuclear charge radii of  $N = 50$  and  $N = 82$  nuclei by using the RMF model with DD-ME2 and DD-PC1 interactions are listed. The results of RMF[NL3\*], HFB with the Skyrme force SLy4 and empirical formula are further listed for comparison. Calculated charge radii of selected nuclei within the framework of relativistic and non-relativistic mean field methods are close to each other. It should be noted that the calculated charge radii values of selected nuclei using the RMF[DD-ME2] interaction are closer to the results of latest refitted empirical charge radii formula given in Eq. (17).

In the present study one may conclude that the RMF model with density-dependent DD-ME2 and DD-PC1 interactions gives close results to the available experimental data for the ground-state nuclear properties of the selected nuclei. The calculated ground-state nuclear properties of  $^{76}\text{Fe}$ ,  $^{78}\text{Ni}$ ,  $^{80}\text{Zn}$ ,  $^{126}\text{Ru}$ ,  $^{128}\text{Pd}$  and  $^{130}\text{Cd}$  using the RMF model, with DD-ME2 and DD-PC1 interactions, are listed in Table 2 and Table 3, respectively. The calculated binding energies, radii of neutron, proton, and charge, deformation parameters and total quadrupole moments ( $Q_T$ ) for selected nuclei are listed in these tables. The calculated ( $S_n$ ,  $S_p$ ,  $S_{2n}$  and  $S_{2p}$ )-separation energies of corresponding waiting points are also listed. The results indicate that these nuclei are close to neutron dripline. It should be noted that the minus sign in the column of  $Q_T$  indicates that this nuclei has oblate shape in its ground-state.

In the present study, we have used the calculated nuclear deformation obtained from the RMF model in our pn-QRPA model as input parameter for the selected nuclei. Because of this reason, we studied the ground-state deformation parameters of these nuclei in detail. For this purpose we have carried out PECs and PESs of the selected nuclei in the RMF model. For PEC calculation, we imposed constraint on the quadrupole moment to calculate binding energy. Later, lowest binding energy was used as reference. Thus, differences between calculated binding energy for specific  $\beta_2$  value and reference binding energy were obtained for carrying out PEC of the related nuclei as a function of  $\beta_2$ . For obtaining PESs of the selected nuclei triaxial shape, both  $\beta$  and  $\gamma$  deformations were taken into account. In this case constraints were used for both of the deformations and the potential energy surfaces in the  $\beta$ - $\gamma$  plane ( $0^\circ \leq \gamma \leq 60^\circ$ ). The PECs and PESs of  $^{76}\text{Fe}$ ,  $^{78}\text{Ni}$ ,  $^{80}\text{Zn}$ ,  $^{126}\text{Ru}$ ,  $^{128}\text{Pd}$  and  $^{130}\text{Cd}$ , obtained by using DD-ME2 and DD-PC1 interactions in the RMF model, are shown in Fig. 4 and Fig. 5, respectively. Contour lines represent a step of 0.75 MeV and the binding energy is set to zero at the minimum of each surface. In our calculations based on the DD-ME2 and DD-PC1 functionals, the PECs of the selected nuclei show a minima around  $\beta_2 = 0$  and the same results are seen in the PESs of the nuclei. These results are consistent with the values of  $\beta_2$  given in Table 2 and Table 3. From this result it may be concluded that RMF model predicts the shapes of  $^{76}\text{Fe}$ ,  $^{78}\text{Ni}$ ,  $^{80}\text{Zn}$ ,  $^{126}\text{Ru}$ ,  $^{128}\text{Pd}$  and  $^{130}\text{Cd}$  to be almost spherical.

After analysis of nuclear ground state properties we next discuss the calculation of weak rates obtained by employing the pn-QRPA model. EE weak rates and EE half-lives of  $^{76}\text{Fe}$ ,  $^{78}\text{Ni}$ ,  $^{80}\text{Zn}$ ,  $^{126}\text{Ru}$ ,  $^{128}\text{Pd}$  and  $^{130}\text{Cd}$  for a wide range of stellar temperature and density were calculated including allowed GT and U1F transitions. The predictive power of our model becomes more effective for smaller half-life values [30, 50] and justifies the implementation of present pn-QRPA model for EE calculation.

Our investigated EE half-lives (GT and GT+U1F) for waiting point isotones with  $N=50$  ( $^{76}\text{Fe}$ ,  $^{78}\text{Ni}$ ,  $^{80}\text{Zn}$ ) is shown in Figure. 6 which consists of three panels. The left and middle panels compare our computed half-lives of allowed GT with GT half-lives of Refs. [56, 62, 63, 64]. In Ref [64], the KHF formula was implemented and two additional types of QRPA calculation, namely QRPA-1 and QRPA-2, were performed. KHF stands for Kratz-Herrmann Formula which was developed by Kratz and Herrmann [65]. They applied the concept of the  $\beta$ -strength function to the integral quantity of the delayed-neutron emission probability and derived a simple phenomenological

expression for the calculation of neutron emission probabilities and half-lives. For details of the model calculation we refer to [64]. The right panel compare the allowed GT+U1F half-lives of our pn-QRPA model with theoretical computations of allowed GT and forbidden contributions of Refs. [35, 63, 66]. In Figure. 7, we show a similar comparison of our calculation for heavy  $N=82$  ( $^{126}\text{Ru}$ ,  $^{128}\text{Pd}$ ,  $^{130}\text{Cd}$ ) waiting point isotones. The left and middle panels of Figure. 7 compare the pn-QRPA model calculated allowed GT half-lives with various theoretical and experimental results. The right panel compares the modified half-lives with inclusion of forbidden contributions. All measured half-lives were taken from [48]. The present computed results for half-life based on the pn-QRPA model for  $N=50$  and  $82$  waiting points are in good comparison with the measured data. The addition of U1F transition resulted in a better comparison of our calculated half-lives with the measured ones. In case of  $N=50$ , the parity changing transitions contribute significantly to the decay rates and hence reduces the total half-lives calculation effectively. For  $N=82$ , the relative contribution of U1F weak rates is comparatively smaller but still significant.

We employed the nuclear deformation parameter ( $\beta_2$ ) values as a free parameter in our calculation. Our first set of computation was based on the  $\beta_2$  values taken from recent globally updated calculation of FRDM [45], which we refer to as pn-QRPA-FRDM. The second and third set of calculations were based on values of  $\beta_2$  computed from the RMF model using density-dependent DD-ME2 and DD-PC1 interactions, respectively. We refer to these calculations as pn-QRPA-RMF[DD-ME2] and pn-QRPA-RMF[DD-PC1], respectively. Table. (4) shows the three set of values of deformation parameter used in our calculation. We first investigated how the computed EE rates changed by using different values of deformation.

In Tables. (5, 6) we display the ratio of calculated pn-QRPA-FRDM to pn-QRPA-RMF[DD-ME2] rates and pn-QRPA-FRDM to pn-QRPA-RMF[DD-PC1] rates, respectively. The ratio includes allowed GT and U1F rates separately. The ratios are computed at  $\rho Y_e = (10^4, 10^7, 10^{11})$  and  $T_9 = (5, 15, 30)$ , where  $\rho Y_e$  and  $T_9$  represent the stellar density and temperature in units of  $g/cm^3$  and  $10^9$  K, respectively. Tables. (5, 6) show that the allowed GT pn-QRPA-FRDM rates are bigger by an order of magnitude than pn-QRPA-RMF[DD-ME2] and pn-QRPA-RMF[DD-PC1] rates for  $^{78}\text{Ni}$  ( $N=50$ ) and  $N=82$  waiting points. For  $^{76}\text{Fe}$  and  $^{80}\text{Zn}$ , the pn-QRPA-FRDM computed allowed GT rates are smaller by the same order of magnitude than the calculated rates by pn-QRPA-RMF[DD-ME2] and pn-QRPA-RMF[DD-PC1].

We note that for larger values of deformation parameters the allowed GT rates are smaller. In case of  $^{130}\text{Cd}$  and  $^{126}\text{Ru}$ , at high stellar density ( $\rho Y_e = 10^{11} \text{ g/cm}^3$ ) and temperature ( $T_9 = 30 \text{ GK}$ ) the ratio of allowed GT for pn-QRPA-FRDM to pn-QRPA-RMF[DD-ME2] and pn-QRPA-RMF[DD-PC1] are an order of magnitude bigger. We further note that all three sets of weak rates increase with increasing temperature and decrease with increasing density values of the core for both GT and U1F transitions. With increasing temperature the number of parent states, that contribute to the total rates, increases. On the other hand, with increasing density the rates start to decrease appreciably due to a decrease in the available phase space. We decided to proceed with the investigation on the total weak rates (Eq. (16)) based only on the pn-QRPA-FRDM model. The reason for this choice was that the FRDM predicts essentially a spherical shape for these closed-shell magic nuclei. We present our results for weak rates using the pn-QRPA-FRDM model in the succeeding paragraphs.

In Tables. (7, 8, 9) we present the computed allowed GT and U1F weak rates for  $N = 50$  waiting point isotones ( $^{76}\text{Fe}$ ,  $^{78}\text{Ni}$  and  $^{80}\text{Zn}$ ) using the pn-QRPA-FRDM model. Similarly in Tables. (10, 11, 12) we show the corresponding results for heavy  $N = 82$  waiting point isotones ( $^{126}\text{Ru}$ ,  $^{128}\text{Pd}$  and  $^{130}\text{Cd}$ ). The computed rates are presented at three different stellar density values of  $10^4 \text{ g/cm}^3$  (representing low-density region),  $10^7 \text{ g/cm}^3$  (representing intermediate-density region) and  $10^{11} \text{ g/cm}^3$  (representing high-density region). The pn-QRPA computed PC and EE rates are shown in logarithmic (to base 10) scale in units of  $s^{-1}$ . We note that the computed PC rates increase as the stellar temperature rises. This makes sense as positrons are created only at high stellar temperatures to get captured. In case of U1F rates one note that the contribution of PC rates are rather significant. Specially at  $T_9 = 30$ , the computed U1F positron capture rates contribute almost 90% for most waiting point isotones. It is evident from Table. (7) to Table. (12) that PC rates must be taken into account, specially at high core temperatures, as they compete well with EE rates for most of the waiting point isotones. Our findings are significant and emphasize that PC rates of waiting point nuclei need to be taken into account in simulation codes, specially at high stellar temperatures.

We next investigate the contribution of U1F rates to the total EE rates using the pn-QRPA-FRDM model. In Figs. (8, 9, 10), we depict the percentage contribution of our computed allowed GT and U1F rates to total EE rates. Fig. 8, Fig. 9 and Fig. 10 are drawn at low ( $\rho Y_e = 10^4 \text{ g/cm}^3$ ),

intermediate ( $\rho Y_e = 10^7 \text{ g/cm}^3$ ) and high ( $\rho Y_e = 10^{11} \text{ g/cm}^3$ ) core density, respectively. Each figure consists of three panels depicting the respective contribution of allowed GT and U1F rates at temperatures  $T_9 = (5, 15 \text{ and } 30)$ . We note that the contribution of U1F rates reduces with increasing stellar density. The U1F electron emission rates contribute reasonably well at low and intermediate stellar densities. We note that for stellar temperatures ( $T_9 \leq 15$ ) and high stellar density values, almost all contribution to total EE rates comes from the GT transitions. The EE rates (GT+U1F) on a fine grid temperature-density scale, suitable for interpolation purposes, are available as ASCII files and may be requested from the corresponding author.

#### 4. Conclusion

In the first investigation of the present study we have used the axially deformed RMF model to calculate the nuclear ground state properties for  $N = 50$  and 82 waiting point isotones. We presented our computations of the ground-state binding energies,  $S_n$ ,  $S_p$ ,  $S_{2n}$ ,  $S_{2p}$ , charge, neutron-proton radii, deformation parameters and quadrupole moments. Two different kinds of density-dependent interactions, namely DD-ME2 and DD-PC1 interactions, were employed in the axially deformed RMF model for the investigation of nuclear ground state properties. The calculated binding energies were found to be in decent agreement with available experimental data. The calculated PECs and PESs of the waiting point isotones show that the ground-state shape of nuclei, studied in this project, are almost spherical.

The second investigation of the present study employed the pn-QRPA model for calculation of weak rates under terrestrial and stellar conditions. EE and PC rates for a wide range of stellar temperature and density were calculated for allowed GT and U1F transitions. Our half-life results were in good agreement with the measured data. The addition of U1F rates appreciably reduced the total calculated half-lives. Our half-life calculation may further be improved by incorporation of non-unique forbidden transitions (rank 0 and 1). We plan to compute non-unique forbidden transitions as a future assignment. We investigated the role of deformation parameter, computed in the RMF model, in our pn-QRPA calculation and concluded that the rates changed by up to an order of magnitude or more by changing the deformation parameters. We further investigated the competition between PC and EE rates. The PC rates on waiting point isotones were found to be significant especially at high core temperatures and low stellar densities. We

noted that contribution of U1F rates are significant to the total EE rates for  $N = 50$  and 82 waiting point isotones. The results presented here might prove useful for the modeling of presupernova evolution of massive stars.

## References

- [1] E.M. Burbidge, G.R. Burbidge, W.A. Fowler, F. Hoyle, *Rev. Mod. Phys.* **29** (1957) 547.
- [2] C.D. Coryell, *J. Chem.* **38** (1961) 67 .
- [3] J.J. Cowan, F.-K. Thielemann, J.W. Truran, *Phys. Rep.* **208** (1991) 267.
- [4] K.-L. Kratz, J.P. Bitouzet, F.-K. Thielemann, P. Möller, B. Pfeiffer, *Astrophys. J.* **403** (1993) 216.
- [5] S.E. Woosley, G.J. Mathews, J.R. Wilson, R.D. Hoffman, B.S. Meyer, *Astrophys. J.* **433** (1994) 229.
- [6] M. Arnould, S. Goriely, and K. Takahashi, *Phys. Rep.* **450** (2007) 97.
- [7] A. Arcones and G. Martínez-Pinedo, *Phys. Rev. C* **83** (2011) 045809.
- [8] S. Furusawa *et al.*, *Phys. Rev. C* **95(2)** (2017) 025809.
- [9] P.T. Hosmer *et al.*, *Phys. Rev. Lett.* **94** (2005) 112501.
- [10] K.-L. Kratz, H. Gabelmann, W. Hillebrandt, B. Pfeiffer, K. Schlösser, F.-K. Thielemann, *Zeitschrift für Physik A Atomic Nuclei* **A 325** (1986) 489.
- [11] B. Pfeiffer, K.-L. Kratz, F.-K. Thielemann, W.B. Walters, *Nucl. Phys.* **A 693** (2001) 282.
- [12] S. Nishimura *et al.*, *Phys. Rev. Lett.* **106** (2011) 052502.
- [13] T. Kurtukian-Nieto *et al.*, *Nucl. Phys. A* **827** (2009) 587C.
- [14] E.M. Ney *et al.*, *Phys. Rev. C* **102** (2020) 034326.
- [15] J. D. Walecka, *Ann. Phys.* **83** (1974) 491.
- [16] J. Boguta, A.R. Bodmer, *Nucl. Phys. A* **292** (1977) 413.



- [17] P. Ring, Prog. Theor. Phys. **37** (1996) 193.
- [18] G.A. Lalazissis, S. Raman, P. Ring, Atom. Data Nucl. Data Tables **71** (1999) 1.
- [19] D. Vretenar, A.V. Afanasjev, G.A. Lalazissis, Phys. Rep. **409** (2005) 101.
- [20] J. Meng, H. Toki, S.G. Zhou, S.Q. Zhang, W.H. Long, L.S. Geng, Prog. Part. Nucl. Phys. **57** (2006) 470.
- [21] Y. K. Gambhir, A. Bhagwat, Phys. Atom. Nucl. **37** (2006) 194.
- [22] A. H. Yilmaz, T. Bayram, J. Korean Phys. Soc. **59** (2011) 3329.
- [23] T. Bayram, A.H. Yilmaz, Mod. Phys. Lett. A. **28** (2013) 1350068.
- [24] T. Bayram, S. Akkoyun, Phys. Scripta. **87** (2013) 065201.
- [25] T. Bayram, S. Akkoyun, Ş. Şentürk, Phys. At. Nucl. **81** (2018) 288.
- [26] T. Bayram, Phys. At. Nucl. **82** (2019) 317.
- [27] H.V. Klapdor-Kleingrothaus, J. Metzinger, T. Oda, At. Data Nucl. Data Tables **31** (1984) 81.
- [28] A. Staudt, E. Bender, K. Muto, H.V. Klapdor-Kleingrothaus, Zeitschrift für Physik A Atomic Nuclei **334** (1989) 47.
- [29] A. Staudt, E. Bender, K. Muto, H.V. Klapdor-Kleingrothaus, At. Data Nucl. Data Tables **44** (1990) 79.
- [30] M. Hirsch, A. Staudt, K. Muto, H.V. Klapdor-Kleingrothaus, At. Data Nucl. Data Tables **53** (1993) 165.
- [31] J.-U. Nabi, H.V. Klapdor-Kleingrothaus, Eur. Phys. J. A **5** (1999) 337.
- [32] J.-U. Nabi, H.V. Klapdor-Kleingrothaus, At. Data Nucl. Data Tables **71** (1999) 149.
- [33] J.-U. Nabi, H.V. Klapdor-Kleingrothaus, At. Data Nucl. Data Tables **88** (2004) 237.

- [34] J.J. Cuenca-García, G. Martínez-Pinedo, K. Langanke, F. Nowacki, I. Borzov, *Eur. Phys. J. A* **34** (2007) 99.
- [35] Q. Zhi, E. Caurier, J.J. Cuenca-García, K. Langanke, G. Martínez-Pinedo, K. Sieja, *Phys. Rev. C* **87** (2013) 025803.
- [36] H. Homma, E. Bender, M. Hirsch, K. Muto, H.V. Klapdor-Kleingrothaus, T. Oda, *Phys. Rev. C* **54** (1996) 2972.
- [37] I.N. Borzov, *Nucl. Phys. A* **777** (2006) 645.
- [38] T. Marketin, L. Huther and G. Martínez-Pinedo, *Phys. Rev. C* **93** (2016) 025805.
- [39] M. Majid, J.-U. Nabi, G. Daraz, *Astrophys. Space Sci.* **362** (2017) 108.
- [40] G. A. Lalazissis, T. Niksic, D. Vretenar, P. Ring, *Phys. Rev. C* **71**, (2005) 024312.
- [41] T. Niksic, N. Paar, D. Vretenar, P. Ring, *Comput. Phys. Commun.* **185** (2014) 1808.
- [42] T. Niksic, D. Vretenar, P. Ring, *Phys. Rev. C* **78** (2008) 034318.
- [43] J. Engel *et al.*, *Phys. Rev. C* **60** (2015) 014302.
- [44] P. Möller, J.R. Nix, W.D. Myers, W.J. Swiatecki, *At. Data Nucl. Data Tables* **59** (1995) 185.
- [45] P. Möller *et al.*, *Atom. Data Nucl. Data Tables* **109-110** (2016) 1-204.
- [46] I. Ragnarsson, R.K. Sheline, *Phys. Ser.* **29** (1984) 385.
- [47] K. Muto, E. Bender and H.V. Klapdor-Kleingrothaus, *Z. Phys. A* **333** (1989) 125.
- [48] G. Audi *et al.*, *Chin. Phys. C* **41** (2017) 030001.
- [49] K. Muto, E. Bender, T. Oda and H.V. Klapdor-Kleingrothaus, *Z. Phys. A* **341** (1992) 407.
- [50] J.-U. Nabi, N. Çakmak, Z. Iftikhar, *Eur. Phys. J. A* **52** (2016) 5.

- [51] J.-U. Nabi, N. Çakmak, S. Stoica, Z. Iftikhar, Phys. Scr. **90** (2015) 115301.
- [52] J.C. Hardy, I.S. Towner, Phys. Rev. C **79** (2009) 055502.
- [53] K. Nakamura [Particle Data Group], J. Phys. G **37** (2010) 075021.
- [54] N.B. Gove, M.J. Martin, At. Data Nucl. Data Tables **10** (1971) 205.
- [55] M.V. Stoitsov, J. Dobaczewski, W. Nazarewicz, S. Pittel, D.J. Dean, Phys. Rev. C **68** (2003) 054312.
- [56] P. Möller, J.R. Nix, K.-L. Kratz, Atom. Data Nucl. Data Tables **66** (1997) 131.
- [57] M. Wang, G. Audi, A.H. Wapstra, F.G. Kondev, M. MacCormick, X. Xu, B. Pfeiffer, Chin. Phys. C **36** (2012) 1603.
- [58] J. Dong, W. Zuo, J. Gu, Phys. Rev. C **91** (2015) 034315.
- [59] G. Fricke *et al.*, At. Data Nucl. Data Tables **60** (1995) 177.
- [60] I. Angeli, K.P. Marinova, At. Data Nucl. Data Tables **99** (2013) 69.
- [61] T. Bayram, S. Akkoyun, S.O. Kara A. Sinan, Acta. Phys. Pol. B **44** (2013) 1791.
- [62] K. Langanke, G. Martínez-Pinedo, Rev. Mod. Phys. **75** (2003) 818.
- [63] P. Möller, B. Pfeiffer, K.-L. Kratz, Phys. Rev. C **67** (2003) 055802.
- [64] B. Pfeiffer, K.-L. Kratz, P. Möller, Prog. Nucl. Energy **41** (2002) 39.
- [65] K.-L. Kratz, G. Herrmann, Zeitschrift für Physik **4263** (1973) 435.
- [66] I.N. Borzov, Phys. Rev. C **71** (2005) 065801.
- [67] G. Martínez-Pinedo, K. Langanke, Phys. Rev. Lett. **83** (1999) 4502.
- [68] P. Hosmer, *et al.*, Phys. Rev. C **82** (2010) 025806.

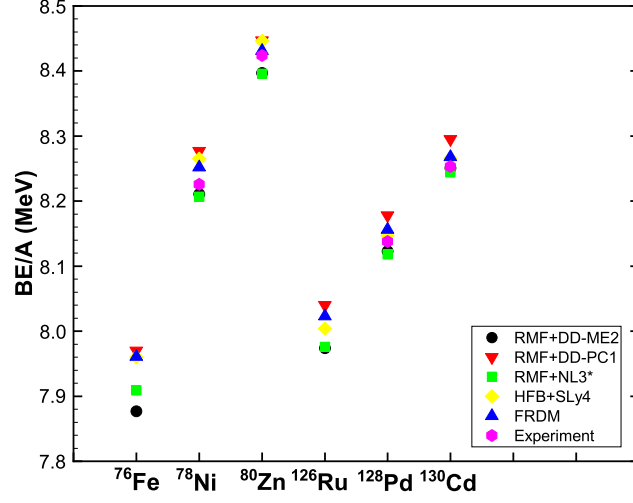


Figure 1: Calculated binding energies per nucleon for  $^{76}\text{Fe}$ ,  $^{78}\text{Ni}$ ,  $^{80}\text{Zn}$ ,  $^{126}\text{Ru}$ ,  $^{128}\text{Pd}$  and  $^{130}\text{Cd}$  using the RMF model with DD-ME2 and DD-PC1 interactions. Results of the RMF model with NL3\* interaction [23], HFB theory with Sly4 parameter set [55], FRDM [45] and available experimental data [57] are also shown for comparison.

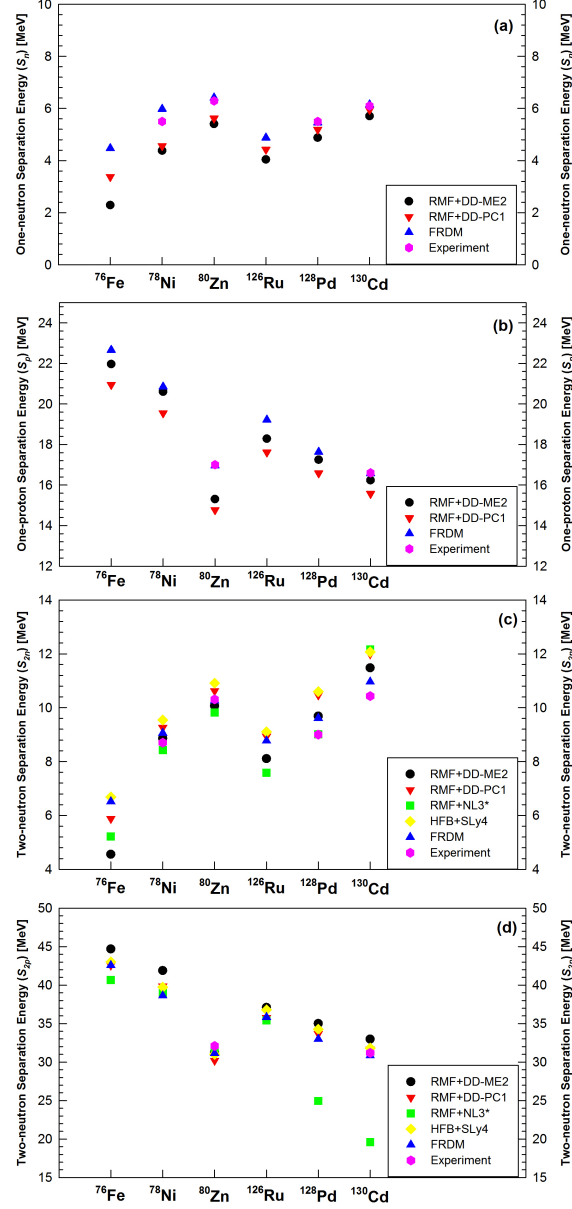


Figure 2: Calculated one-neutron (a), one-proton (b), two-neutron (c) and two-proton (d) separation energies for  $^{76}\text{Fe}$ ,  $^{78}\text{Ni}$ ,  $^{80}\text{Zn}$ ,  $^{126}\text{Ru}$ ,  $^{128}\text{Pd}$  and  $^{130}\text{Cd}$  using the RMF model with DD-ME2 and DD-PC1 interactions. Available theoretical predictions from the RMF model with NL3\* interaction [23], HFB theory with Sly4 parameter set [55], FRDM [45] and experimental data [57] are also shown for comparison.

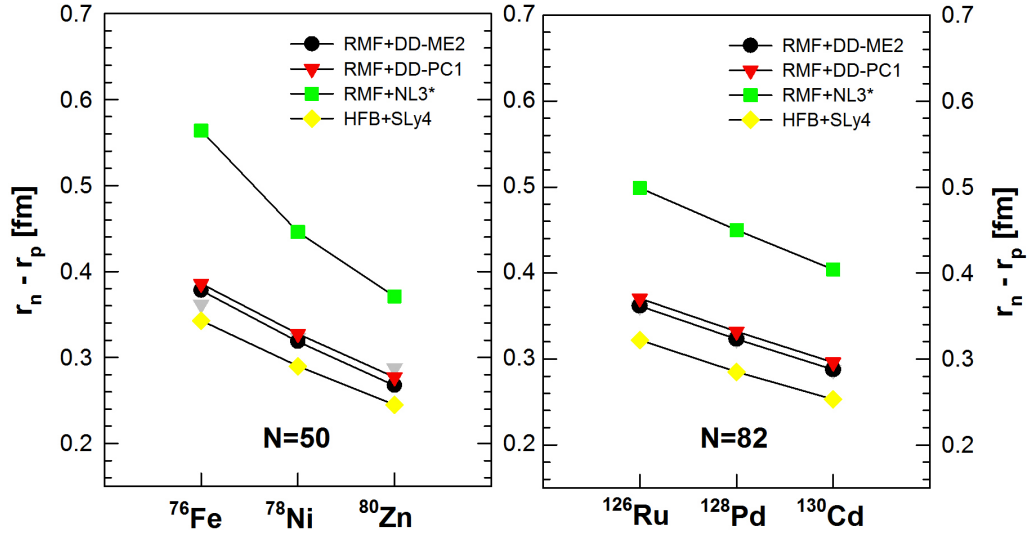


Figure 3: Calculated neutron skin thickness for  $^{76}\text{Fe}$ ,  $^{78}\text{Ni}$ ,  $^{80}\text{Zn}$ ,  $^{126}\text{Ru}$ ,  $^{128}\text{Pd}$  and  $^{130}\text{Cd}$  using the RMF model with DD-ME2 and DD-PC1 interactions. Results of the RMF model with NL3\* interaction [23] and HFB theory with Sly4 interaction [55] are also shown for comparison.

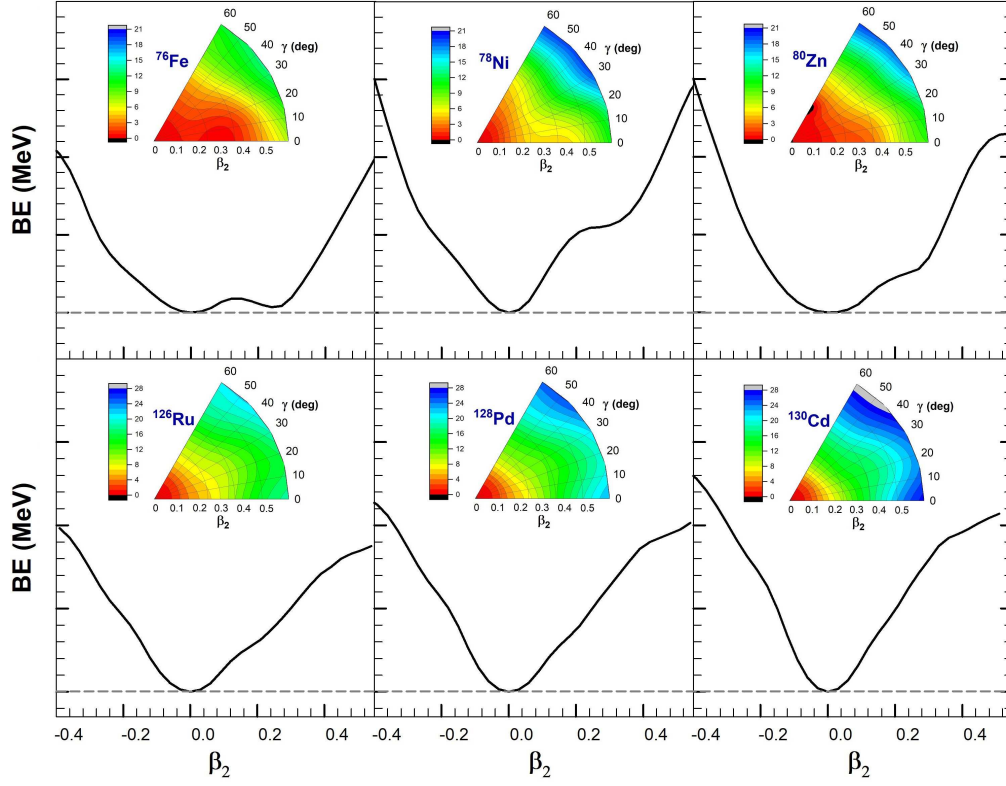


Figure 4: Calculated PECs and PESs for  $^{76}\text{Fe}$ ,  $^{78}\text{Ni}$ ,  $^{80}\text{Zn}$ ,  $^{126}\text{Ru}$ ,  $^{128}\text{Pd}$  and  $^{130}\text{Cd}$  using the RMF model with DD-ME2 interaction.

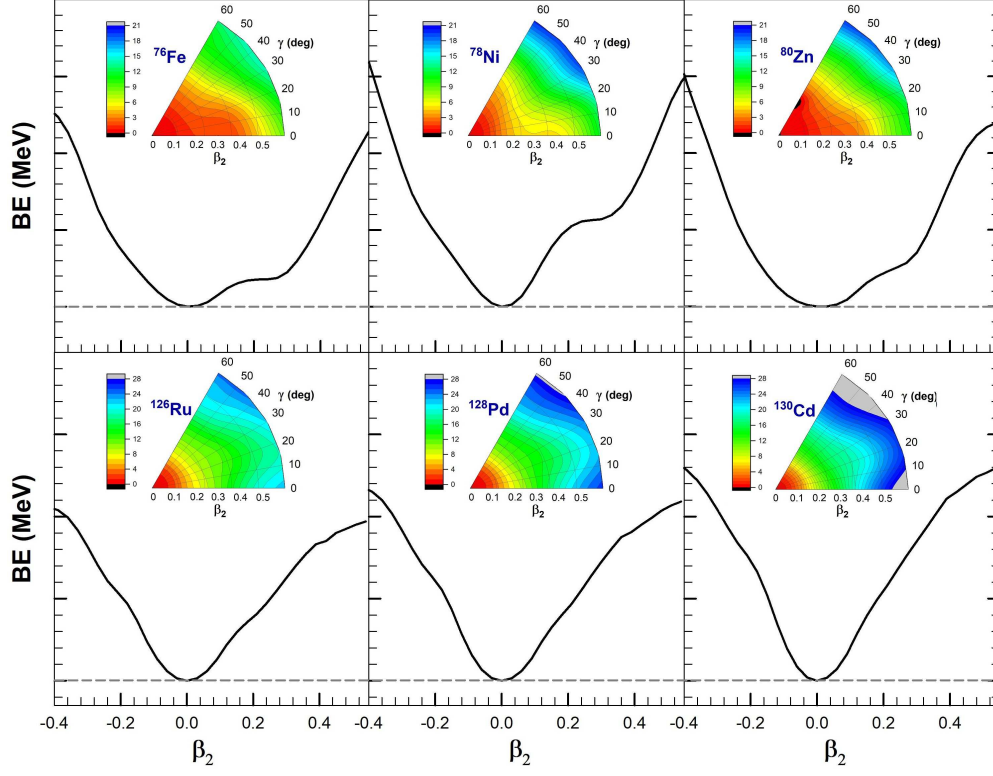


Figure 5: Calculated PECs and PESs for  $^{76}\text{Fe}$ ,  $^{78}\text{Ni}$ ,  $^{80}\text{Zn}$ ,  $^{126}\text{Ru}$ ,  $^{128}\text{Pd}$  and  $^{130}\text{Cd}$  using the RMF model with DD-PC1 interaction.



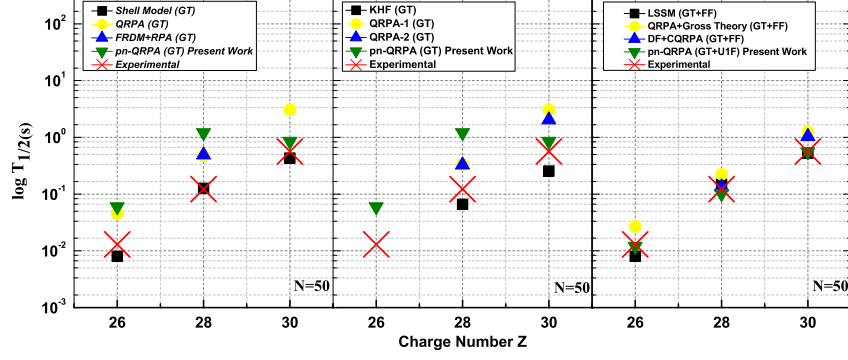


Figure 6: Calculated and measured electron emission half-lives of  $N = 50$  waiting point isotones. The right panel depicts the results of Shell Model (GT) [62], QRPA (GT) [63] and FRDM+RPA (GT) [56], the middle panel shows the theoretical computations of KHF, QRPA-1 and QRPA-2 [64]. The right panel depicts the results of LSSM (GT+FF) [35], QRPA+Gross theory (GT+FF) [63] and DF-CQRPA (GT+FF) [66]. Allowed GT pn-QRPA calculation is shown as GT while those including unique first-forbidden contribution as (GT+U1F). Experimental values were taken from Ref. [48].

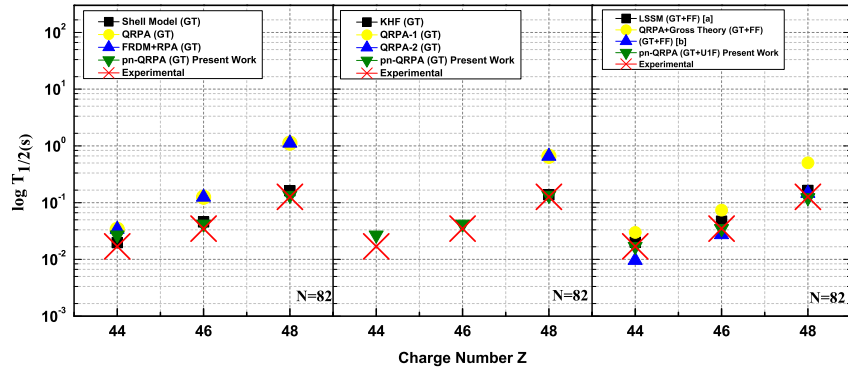


Figure 7: Calculated and measured electron emission half-lives of  $N = 82$  waiting point isotones. The right panel depicts the results of Shell model (GT) [34], QRPA (GT) [63] and FRDM+RPA (GT) [56], the middle panel shows the theoretical calculations of KHF, QRPA-1 and QRPA-2 [64]. The right panel shows the results of LSSM (GT+FF) [a]  $\rightarrow$  [35], QRPA+Gross theory (GT+FF) [63] and GT+FF results [b]  $\rightarrow$  [67]. Allowed GT pn-QRPA calculation is shown as GT while those including unique first-forbidden contribution as (GT+U1F). Experimental values were taken from Ref. [48].

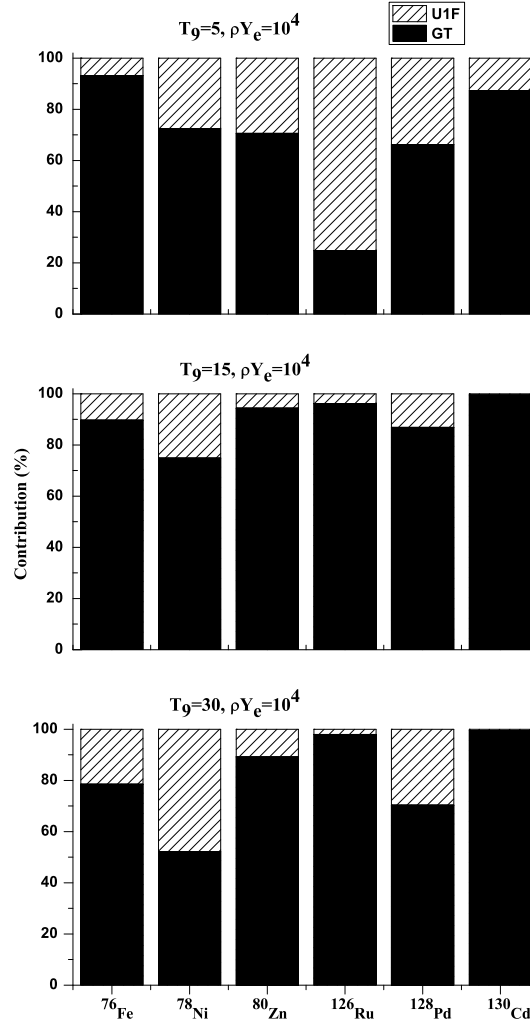


Figure 8: Percentage contribution of allowed GT and U1F rates to total electron emission  $\lambda_{EE}$  rates. Stellar density  $\rho Y_e$  is stated in units of  $g/cm^3$ , while temperature  $T_9$  is given in units of  $10^9 K$ .

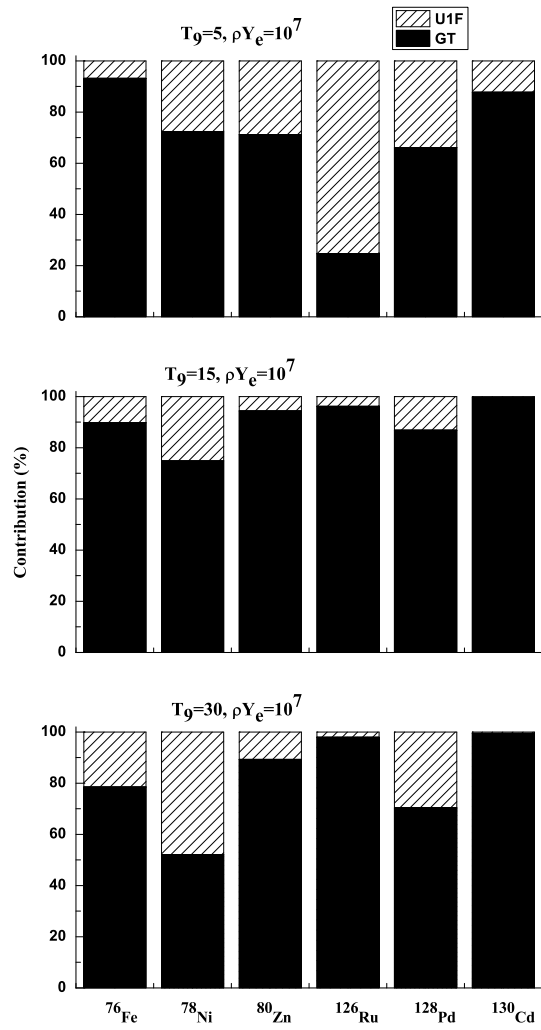


Figure 9: Same as Figure. 8 but for stellar density  $10^7 g/cm^3$ .

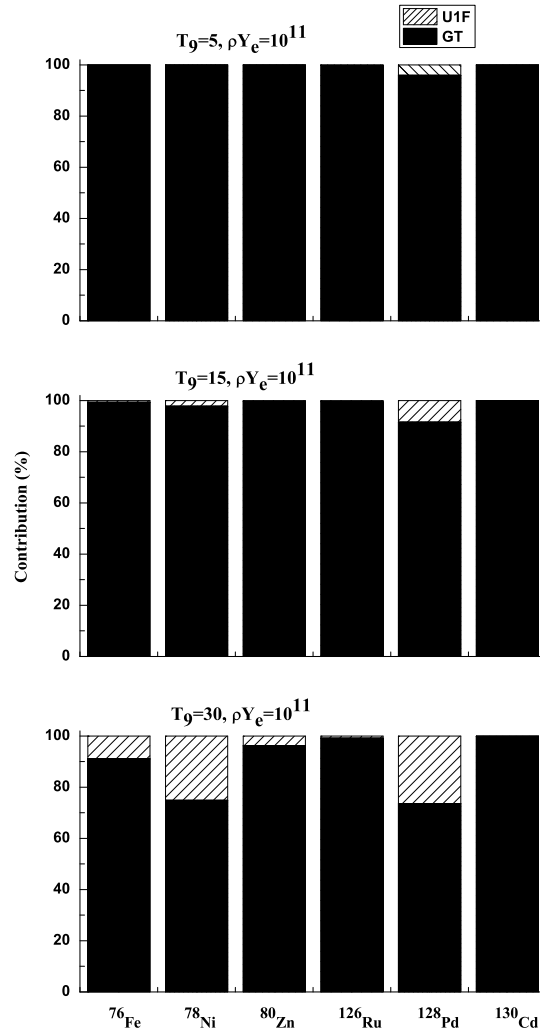


Figure 10: Same as Figure. 8 but for stellar density  $10^{11} g/cm^3$ .

Table 1: Calculated charge radii of  $^{76}\text{Fe}$ ,  $^{78}\text{Ni}$ ,  $^{80}\text{Zn}$ ,  $^{126}\text{Ru}$ ,  $^{128}\text{Pd}$  and  $^{130}\text{Cd}$  using the RMF model with DD-ME2 and DD-PC1 interactions in comparison with HFB and empirical results. All units are in  $fm$ .

Nucleus	RMF[DD-ME2]	RMF[DD-PC1]	RMF[NL3*] [23]	HFB[SLy4] [55]	Empirical [61]
$^{76}\text{Fe}$	3.924	3.936	3.787	3.956	3.818
$^{78}\text{Ni}$	3.964	3.979	3.979	4.004	3.906
$^{80}\text{Zn}$	4.023	4.039	4.038	4.055	3.991
$^{126}\text{Ru}$	4.630	4.629	4.646	4.639	4.500
$^{128}\text{Pd}$	4.661	4.663	4.676	4.674	4.564
$^{130}\text{Cd}$	4.691	4.695	4.705	4.706	4.626

Table 2: Calculated ground-state properties of  $^{76}\text{Fe}$ ,  $^{78}\text{Ni}$ ,  $^{80}\text{Zn}$ ,  $^{126}\text{Ru}$ ,  $^{128}\text{Pd}$  and  $^{130}\text{Cd}$  using the RMF model with DD-ME2 interaction.

Nuclei	BE/A [MeV]	$S_n$ [MeV]	$S_p$ [MeV]	$S_{2n}$ [MeV]	$S_{2p}$ [MeV]	$r_n$ [fm]	$r_p$ [fm]	$r_c$ [fm]	$\beta_2$	$Q_T$ [barn]
$^{76}\text{Fe}$	7.877	2.288	21.963	4.554	44.674	4.219	3.841	3.924	0.0001	0.001
$^{78}\text{Ni}$	8.211	4.379	20.596	8.856	41.878	4.198	3.880	3.961	0.0004	0.006
$^{80}\text{Zn}$	8.397	5.403	15.302	10.065	31.265	4.210	3.942	4.023	0.0012	0.020
$^{126}\text{Ru}$	7.974	4.040	18.280	8.103	37.093	4.922	4.561	4.630	-0.0014	-0.048
$^{128}\text{Pd}$	8.123	4.875	17.244	9.683	35.002	4.915	4.592	4.661	-0.0015	-0.054
$^{130}\text{Cd}$	8.251	5.703	16.232	11.476	32.968	4.909	4.622	4.691	-0.0015	-0.054

Table 3: Same as Table 2 but for RMF model with DD-PC1 interaction.

Nuclei	BE/A [MeV]	$S_n$ [MeV]	$S_p$ [MeV]	$S_{2n}$ [MeV]	$S_{2p}$ [MeV]	$r_n$ [fm]	$r_p$ [fm]	$r_c$ [fm]	$\beta_2$	$Q_T$ [barn]
$^{76}\text{Fe}$	7.970	3.377	20.947	5.879	42.581	4.240	3.854	3.936	-0.0001	-0.002
$^{78}\text{Ni}$	8.277	4.564	19.545	9.259	39.858	4.225	3.898	3.979	-0.0011	-0.017
$^{80}\text{Zn}$	8.447	5.619	14.769	10.625	30.201	4.236	3.959	4.039	-0.0058	-0.095
$^{126}\text{Ru}$	8.040	4.425	17.613	8.932	35.755	4.930	4.559	4.629	-0.0008	-0.026
$^{128}\text{Pd}$	8.178	5.189	16.584	10.465	33.679	4.926	4.594	4.663	-0.0011	-0.039
$^{130}\text{Cd}$	8.295	5.950	15.572	11.991	31.650	4.923	4.627	4.695	-0.0013	-0.047

Table 4: Calculated deformation parameters ( $\beta_2$ ) used by pn-QRPA calculation from FRDM [45] and those deduced from the RMF model with DDME2 and DDPC1 interactions.

Nuclei	$\beta_2$ (FRDM)	$\beta_2$ (RMF[DD-ME2])	$\beta_2$ (RMF[DD-PC1])
$^{76}\text{Fe}$	-0.01100	0.00010	-0.00010
$^{78}\text{Ni}$	0.00000	0.00040	-0.00110
$^{80}\text{Zn}$	-0.01000	0.00120	-0.00580
$^{126}\text{Ru}$	0.00000	-0.00140	-0.00080
$^{128}\text{Pd}$	0.00000	-0.00150	-0.00110
$^{130}\text{Cd}$	0.00000	-0.00150	-0.00130

Table 5: Ratio of computed (allowed GT and U1F electron emission ( $\lambda_{EE}$ )) pn-QRPA-FRDM to pn-QRPA-RMF[DD-ME2] rates as a function of stellar temperature and density. Stellar temperature ( $T_9$ ) and density ( $\rho Y_e$ ) are shown in units of  $10^9 K$  and  $g/cm^3$ , respectively.

Nucleus	$T_9$	Ratio [Allowed GT]			Ratio [U1F]		
		$\rho Y_e=10^4$	$\rho Y_e=10^7$	$\rho Y_e=10^{11}$	$\rho Y_e=10^4$	$\rho Y_e=10^7$	$\rho Y_e=10^{11}$
$^{76}\text{Fe}$	5	5.62E-01	5.62E-01	5.66E-01	1.38E+00	1.38E+00	3.50E+00
	15	2.40E-01	2.40E-01	2.42E-01	1.66E+00	1.66E+00	3.78E+00
	30	1.21E-01	1.21E-01	1.17E-01	2.09E+00	2.09E+00	4.26E+00
$^{78}\text{Ni}$	5	1.00E+00	1.00E+00	1.32E+00	9.89E-01	9.89E-01	8.53E-01
	15	2.26E+00	2.26E+00	4.24E+00	8.47E-01	8.47E-01	7.73E-01
	30	4.11E+00	4.11E+00	5.38E+00	6.32E-01	6.32E-01	6.00E-01
$^{80}\text{Zn}$	5	9.44E-01	9.44E-01	9.89E-01	1.02E+00	1.03E+00	1.04E+00
	15	7.69E-01	7.71E-01	9.66E-01	1.03E+00	1.04E+00	1.06E+00
	30	6.18E-01	6.19E-01	6.95E-01	1.09E+00	1.09E+00	1.09E+00
$^{126}\text{Ru}$	5	1.16E+00	1.15E+00	3.30E+00	9.55E-01	9.62E-01	2.05E-01
	15	6.43E+00	6.43E+00	3.84E+00	9.51E-01	9.31E-01	2.04E-01
	30	7.64E+00	7.62E+00	6.14E+00	8.59E-01	9.18E-01	1.99E-01
$^{128}\text{Pd}$	5	2.31E+00	2.32E+00	1.11E+00	9.42E-01	9.35E-01	8.20E-01
	15	2.52E+00	2.52E+00	1.46E+00	8.89E-01	8.89E-01	5.04E-01
	30	2.56E+00	2.56E+00	1.51E+00	4.66E-01	4.67E-01	3.90E-01
$^{130}\text{Cd}$	5	1.22E+00	1.23E+00	5.92E+01	9.82E-01	9.84E-01	8.09E-01
	15	1.96E+01	1.97E+01	7.01E+01	3.31E-01	3.31E-01	2.94E-01
	30	2.12E+01	2.12E+01	3.73E+01	1.94E-01	1.94E-01	1.83E-01

Table 6: Ratio of computed (allowed GT and U1F electron emission ( $\lambda_{EE}$ )) pn-QRPA-FRDM to pn-QRPA-RMF[DD-PC1] rates as a function of stellar temperature and density. Stellar temperature ( $T_9$ ) and density ( $\rho Y_e$ ) are shown in units of  $10^9 K$  and  $g/cm^3$ , respectively.

Nucleus	$T_9$	Ratio [Allowed GT]			Ratio [U1F]		
		$\rho Y_e=10^4$	$\rho Y_e=10^7$	$\rho Y_e=10^{11}$	$\rho Y_e=10^4$	$\rho Y_e=10^7$	$\rho Y_e=10^{11}$
$^{76}\text{Fe}$	5	5.62E-01	5.62E-01	5.66E-01	1.38E+00	1.38E+00	3.53E+00
	15	2.40E-01	2.40E-01	2.42E-01	1.66E+00	1.66E+00	3.78E+00
	30	1.21E-01	1.21E-01	1.17E-01	2.09E+00	2.09E+00	4.26E+00
$^{78}\text{Ni}$	5	1.01E+00	1.01E+00	1.16E+00	9.89E-01	9.89E-01	8.53E-01
	15	2.33E+00	2.33E+00	4.23E+00	8.05E-01	8.05E-01	7.53E-01
	30	5.05E+00	5.05E+00	6.64E+00	6.12E-01	6.12E-01	5.83E-01
$^{80}\text{Zn}$	5	9.77E-01	9.77E-01	7.33E-01	1.01E+00	1.01E+00	1.05E+00
	15	8.34E-01	8.30E-01	6.14E-01	1.01E+00	1.01E+00	1.07E+00
	30	7.18E-01	7.18E-01	6.04E-01	1.02E+00	1.03E+00	1.15E+00
$^{126}\text{Ru}$	5	1.13E+00	1.12E+00	9.82E+00	9.62E-01	9.62E-01	8.17E-01
	15	9.20E+00	9.20E+00	9.31E+00	9.51E-01	9.57E-01	5.75E-01
	30	9.40E+00	9.40E+00	1.01E+01	9.40E-01	9.20E-01	2.56E-01
$^{128}\text{Pd}$	5	2.38E+00	2.39E+00	1.82E+00	9.46E-01	9.38E-01	8.20E-01
	15	2.40E+00	2.40E+00	1.96E+00	8.69E-01	8.69E-01	5.01E-01
	30	2.46E+00	2.52E+00	2.03E+00	4.49E-01	4.49E-01	3.94E-01
$^{130}\text{Cd}$	5	1.22E+00	1.22E+00	7.13E+01	9.95E-01	9.95E-01	8.45E-01
	15	2.03E+01	2.04E+01	7.48E+01	3.28E-01	3.28E-01	2.88E-01
	30	2.15E+01	2.15E+01	3.84E+01	1.86E-01	1.86E-01	1.74E-01

Table 7: Computed allowed GT and U1F positron capture ( $\lambda_{PC}$ ) and electron emission ( $\lambda_{EE}$ ) rates on  $^{76}\text{Fe}$ .  $\%_{PC}$  and  $\%_{EE}$  represent the percentage contribution of  $\lambda_{PC}$  and  $\lambda_{EE}$  rates, respectively, to the total rate.  $\rho Y_e$  and  $T_9$  are stated in units of  $g/cm^3$  and  $10^9 K$ , respectively. Rates are stated in logarithmic (to base 10) scale in units of  $s^{-1}$ .

$\rho Y_e$	$T_9$	$^{76}\text{Fe}$ [Allowed GT]				$^{76}\text{Fe}$ [U1F]			
		$\lambda_{PC}(s^{-1})$	$\lambda_{EE}(s^{-1})$	$\%_{PC}$	$\%_{EE}$	$\lambda_{PC}(s^{-1})$	$\lambda_{EE}(s^{-1})$	$\%_{PC}$	$\%_{EE}$
$10^4$	5	-1.62	1.46	0.08	99.92	-1.21	1.53	0.18	99.82
	15	0.42	1.75	4.43	95.57	1.48	1.93	26.01	73.99
	30	1.80	1.96	41.00	59.00	3.62	2.43	93.88	6.12
$10^7$	5	-2.30	1.45	0.02	99.98	-1.91	1.53	0.04	99.96
	15	0.39	1.75	4.17	95.83	1.45	1.93	24.83	75.17
	30	1.80	1.96	40.84	59.16	3.61	2.43	93.84	6.16
$10^{11}$	5	-25.70	-10.53	0.00	100.00	-25.30	-14.34	0.00	100.00
	15	-7.52	-2.69	0.00	100.00	-6.47	-4.01	0.34	99.66
	30	-2.04	-0.41	2.26	97.74	-0.24	-0.46	62.56	37.44

Table 8: Same as Table. 7 but for  $^{78}\text{Ni}$ .

$\rho Y_e$	$T_9$	$^{78}\text{Ni}$ [Allowed GT]				$^{78}\text{Ni}$ [U1F]			
		$\lambda_{PC}(s^{-1})$	$\lambda_{EE}(s^{-1})$	$\%_{PC}$	$\%_{EE}$	$\lambda_{PC}(s^{-1})$	$\lambda_{EE}(s^{-1})$	$\%_{PC}$	$\%_{EE}$
$10^4$	5	-1.99	0.53	0.30	99.70	-1.45	0.81	0.54	99.46
	15	0.52	1.58	8.05	91.95	1.22	1.07	58.49	41.51
	30	2.28	2.26	51.55	48.45	3.48	1.45	99.06	0.94
$10^7$	5	-2.67	0.52	0.06	99.94	-2.15	0.81	0.11	99.89
	15	0.50	1.58	7.61	92.39	1.19	1.07	57.03	42.97
	30	2.28	2.26	51.44	48.56	3.47	1.45	99.06	0.94
$10^{11}$	5	-26.06	-15.54	0.00	100.00	-25.54	-17.95	0.00	100.00
	15	-7.41	-3.43	0.01	99.99	-6.73	-5.39	4.35	95.65
	30	-1.56	-0.26	4.79	95.21	-0.38	-1.64	94.78	5.22

Table 9: Same as Table. 7 but for  $^{80}\text{Zn}$ .

$\rho Y_e$	$T_9$	$^{80}\text{Zn}$ [Allowed GT]				$^{80}\text{Zn}$ [U1F]			
		$\lambda_{PC}(s^{-1})$	$\lambda_{EE}(s^{-1})$	$\%_{PC}$	$\%_{EE}$	$\lambda_{PC}(s^{-1})$	$\lambda_{EE}(s^{-1})$	$\%_{PC}$	$\%_{EE}$
$10^4$	5	-2.21	-0.09	0.75	99.25	-1.73	-0.47	5.24	94.76
	15	0.43	1.33	11.09	88.91	1.22	-0.03	94.58	5.42
	30	1.83	1.53	66.61	33.39	3.55	0.46	99.92	0.08
$10^7$	5	-2.90	-0.10	0.16	99.84	-2.42	-0.49	1.17	98.83
	15	0.40	1.33	10.51	89.49	1.19	-0.03	94.29	5.71
	30	1.82	1.53	66.46	33.54	3.55	0.46	99.92	0.08
$10^{11}$	5	-26.29	-16.74	0.00	100.00	-25.81	-21.27	0.00	100.00
	15	-7.51	-4.32	0.06	99.94	-6.74	-7.02	65.74	34.26
	30	-2.02	-1.25	14.57	85.43	-0.31	-2.83	99.70	0.30

Table 10: Same as Table. 7 but for  $^{126}\text{Ru}$ .

$\rho Y_e$	$T_9$	$^{126}\text{Ru}$ [Allowed GT]				$^{126}\text{Ru}$ [U1F]			
		$\lambda_{PC}(s^{-1})$	$\lambda_{EE}(s^{-1})$	% $_{PC}$	% $_{EE}$	$\lambda_{PC}(s^{-1})$	$\lambda_{EE}(s^{-1})$	% $_{PC}$	% $_{EE}$
$10^4$	5	-1.98	1.08	0.09	99.91	-1.10	2.14	0.06	99.94
	15	1.34	3.02	2.07	97.93	1.64	2.22	20.98	79.02
	30	2.77	3.27	23.90	76.10	3.63	2.48	93.30	6.70
$10^7$	5	-2.67	1.07	0.02	99.98	-1.80	2.14	0.01	99.99
	15	1.32	3.02	1.95	98.05	1.62	2.22	20.00	80.00
	30	2.76	3.27	23.82	76.18	3.62	2.48	93.26	6.74
$10^{11}$	5	-26.06	-12.07	0.00	100.00	-25.19	-14.59	0.00	100.00
	15	-6.59	-1.89	0.00	100.00	-6.31	-3.76	0.28	99.72
	30	-1.08	0.77	1.41	98.59	-0.23	-0.50	65.22	34.78

Table 11: Same as Table. 7 but for  $^{128}\text{Pd}$ .

$\rho Y_e$	$T_9$	$^{128}\text{Pd}$ [Allowed GT]				$^{128}\text{Pd}$ [U1F]			
		$\lambda_{PC}(s^{-1})$	$\lambda_{EE}(s^{-1})$	% $_{PC}$	% $_{EE}$	$\lambda_{PC}(s^{-1})$	$\lambda_{EE}(s^{-1})$	% $_{PC}$	% $_{EE}$
$10^4$	5	-1.40	1.77	0.07	99.93	-1.85	1.48	0.05	99.95
	15	1.11	2.48	4.08	95.92	0.86	1.66	13.63	86.37
	30	2.28	2.55	34.94	65.06	2.78	1.94	87.37	12.63
$10^7$	5	-2.08	1.77	0.01	99.99	-2.55	1.47	0.01	99.99
	15	1.08	2.48	3.85	96.15	0.83	1.66	12.91	87.09
	30	2.28	2.55	34.73	65.27	2.77	1.94	87.27	12.73
$10^{11}$	5	-25.47	-14.38	0.00	100.00	-25.94	-15.76	0.00	100.00
	15	-6.83	-3.29	0.03	99.97	-7.09	-4.33	0.17	99.83
	30	-1.57	-0.51	8.01	91.99	-1.08	-0.95	42.63	57.37

Table 12: Same as Table. 7 but for  $^{130}\text{Cd}$ .

$\rho Y_e$	$T_9$	$^{130}\text{Cd}$ [Allowed GT]				$^{130}\text{Cd}$ [U1F]			
		$\lambda_{PC}(s^{-1})$	$\lambda_{EE}(s^{-1})$	% $_{PC}$	% $_{EE}$	$\lambda_{PC}(s^{-1})$	$\lambda_{EE}(s^{-1})$	% $_{PC}$	% $_{EE}$
$10^4$	5	-2.12	0.62	0.18	99.82	-2.08	-0.57	3.01	96.99
	15	1.03	2.47	3.48	96.52	0.90	-0.28	93.82	6.18
	30	2.47	2.67	38.69	61.31	3.00	0.02	99.90	0.10
$10^7$	5	-2.81	0.61	0.04	99.96	-2.77	-0.60	0.67	99.33
	15	1.00	2.47	3.28	96.72	0.87	-0.29	93.50	6.50
	30	2.47	2.67	38.47	61.53	3.00	0.02	99.89	0.11
$10^{11}$	5	-26.20	-15.74	0.00	100.00	-26.17	-21.93	0.01	99.99
	15	-6.91	-3.12	0.02	99.98	-7.05	-7.38	67.83	32.17
	30	-1.37	-0.08	4.80	95.20	-0.86	-3.31	99.65	0.35